

## Shaping and manipulation of light fields with bottom-up plasmonic structures

C Girard<sup>1</sup>, E Dujardin<sup>1</sup>, G Baffou<sup>2</sup> and R Quidant<sup>2</sup>

<sup>1</sup> Nanoscience Group, CEMES, UPR-CNRS 8011, 29 Rue Jeanne Marvig, 31055 Toulouse, France

<sup>2</sup> ICFO–Institut de Ciències Fotoniques, Mediterranean Technology Park, 08860 Castelldefels, Barcelona, Spain

E-mail: [girard@cemes.fr](mailto:girard@cemes.fr)

*New Journal of Physics* **10** (2008) 105016 (22pp)

Received 23 May 2008

Published 28 October 2008

Online at <http://www.njp.org/>

doi:10.1088/1367-2630/10/10/105016

**Abstract.** A new interdisciplinary topic which aims at self-assembling, interconnecting and characterizing resonant metallic nanostructures able to funnel, confine, and propagate light energy from a conventional laser source to a single molecular entity is currently emerging in different laboratories. With this technique, several orders of magnitude in the miniaturization scale of optical devices, spanning from tens of micrometres down to the molecular scale, can be expected. With the main objective of overcoming the current limitations of an exclusive top-down approach to plasmonics, we present in this paper some recent experimental and theoretical results about plasmonic structures made by self-assembling or surface deposition of colloidal metallic particles. More specifically, the interest of these objects for tailoring original near-field optical properties will be exposed (near-field optical confinement, local density of electromagnetic state squeezing, etc). In particular, it is shown that a bottom-up approach is not only able to produce interesting nanoscale building blocks but also able to easily produce complex superstructures that would be difficult to achieve by other means.

**Contents**

<b>1. Introduction</b>	<b>2</b>
<b>2. Bottom-up fabrication methods</b>	<b>3</b>
2.1. Synthesis of self-assembled plasmonic nanoparticle networks (PNNs) . . . . .	4
2.2. Deposition on dielectric surfaces . . . . .	6
<b>3. Near-field optical properties of self-assembled plasmonics</b>	<b>8</b>
3.1. A GDM for the submicrometre scale . . . . .	8
3.2. CDA approach of the nanometre scale . . . . .	17
<b>4. Conclusion and perspective</b>	<b>20</b>
<b>Acknowledgments</b>	<b>20</b>
<b>References</b>	<b>20</b>

**1. Introduction**

Microelectronics overall supremacy over data storage and processing can, in part, be attributed to a successful pace in miniaturizing its elementary components while maintaining or even improving their performance for the past 60 years. However, power dissipation in current and future generations of transistors and interconnects has gradually appeared as a major concern for electron-based information technology. While numerous alternatives have been proposed, none has yet achieved the same level of maturity and consistency but photonics is now recognized as a performing partner to microelectronics. In this regard, conventional photonics lacks spatial resolution, but the conversion of photon energy to plasmonic excitation using noble metal surfaces opens up a new realm below the usual diffraction limit of light (Barnes *et al* 2003, Berini 2000, Charbonneau *et al* 2000, Krenn *et al* 1999a, 1999b, Weeber *et al* 2001). The newborn research field of plasmonics (Christ *et al* 2007, 2008, Devaux *et al* 2003, Félidj *et al* 2002, Girard 2005, Girard and Quidant 2004, Klar *et al* 1998, Krenn *et al* 1997, 2002, Lévêque and Martin 2008, Linden *et al* 2001, Maier *et al* 2001, 2002, Passian *et al* 2004, Smolyaninov *et al* 1996, Wiederrecht 2004, Wurtz *et al* 2003, Zayats and Smolyaninov 2003) proposes alternative approaches for the fabrication of the next generation of photonic components (Bozhevolnyi *et al* 2001) with new industrial developments in various application domains of nano-optics: optical communication, bio-chemical sensing and light generation, and imaging but also in opto-electronics and high density optical storage. However, conventional plasmonics is currently facing a major challenge that would benefit from a bottom-up strategy, such as colloid self-assembly. Indeed, spatial control (dimensions and definition of shapes and interstices) and energy dissipation are limiting the performance of microfabricated plasmonic devices made of amorphous or highly polycrystalline evaporated metallic features with a minimal lateral dimension of typically 100 nm. Furthermore, any application of plasmonics will rely on cheap structuring routines which necessarily need to be parallel.

By combining different self-assembling and self-organizing (bottom-up) approaches with lithography, nano-inking and other top-down methods, it becomes conceivable to produce integrated multiscale plasmonic architectures able to channel light from a micron-sized laser beam to nanoscopic entities. The fabricated architectures can be optically characterized at the different scale levels by suitable far-field, near-field (Dickson and Lyon 2000, Girard *et al* 2006, Imura *et al* 2004a, 2004b, 2004c), single molecule methods (Frey *et al* 2004, Gerton *et al* 2004)

or electron energy loss spectroscopy (EELS) methods (Garcia de Abajo and Kociak 2008, Nelayah *et al* 2007). From these new systems, specific key applications such as ultra-sensitive sensors, ultra-small interconnects, enhanced spectroscopy and nanoscale microscopy could be tested.

In the following section of this paper, we report on recent experimental advances in the fabrication of optically relevant plasmonics nanostructures. Higher-order architectures are obtained by spontaneous self-assembly which yields, for example, metal nanoparticle short chains or extended networks. We foresee that the diversity of colloidal chemistry principles that can be applied to such systems will not only allow the design and production of well-defined superstructures such as dimers, trimers, short chains with controlled length and topology but also offer a versatile platform for post-assembly functionalization with active molecular moieties.

The investigation of fundamental aspects and the optimization of the functionalities of bottom-up plasmonic superstructures described in section 2 require an intensive support of both theoretical modeling and numerical simulations. For example, understanding how plasmons couple with each other and with nearby molecules (Azoulay *et al* 2000, Barnes 1998, Frey *et al* 2004) will be one of the major questions associated with future *bottom-up plasmonics* (Baffou *et al* 2008, Bennett *et al* 2001). Among several challenging theoretical objectives, we can mention (i) accurate evaluation of dissipation in the developed multiscale plasmonic structures; (ii) study of the consequences of disorder on the efficiency of self-assembled plasmonic architectures; and (iii) a realistic description of molecular coupling with plasmonic surroundings.

The third section of this paper will be devoted to the development of items (i) and (ii). For realizing these objectives, numerical tools mainly based on the Green dyadic method (GDM) will enable us to compute accurately the local electromagnetic properties of supported three-dimensional (3D) metal superstructures with complex geometries lying on a substrate. Interestingly, the molecular scale can be investigated from methodologies borrowed from different domains of optical physics. At this scale, optical Bloch equations methods can be satisfactorily coupled with both GDM as well as coupled dipole approximation (CDA) schemes. In particular, they can be efficient to study photophysical effects such as molecular fluorescence, triggered in the vicinity of plasmonic particles for arbitrary profile, wavelength, optical index and surrounding geometry (Colas des Francs *et al* 2003, Das and Metiu 1982).

## 2. Bottom-up fabrication methods

While colloidal chemists and materials scientists have studied the optical properties of suspensions of finely divided metals for several decades, the design of these properties by tailoring the shape and size of metal nanoparticles has only become a topic of interest recently. The next level of subtlety is the control of coupling between localized surface plasmons (LSP) by mastering the spatial organization of nanoparticles, which is still the focus of intense research. Although these two aspects would deserve in-depth considerations, the reader is invited to refer to recent reviews on shape control of metallic nanoparticles (Tao *et al* 2008) and on superstructure formation by nanoparticle self-assembly (Kinge *et al* 2008, Zhang *et al* 2006). In the following section, we will illustrate how chemists can now create colloidal superstructures of interest for physicists to be able to integrate and study future generations of plasmonic devices.

### 2.1. Synthesis of self-assembled plasmonic nanoparticle networks (PNNs)

Colloidal stability results from the balance between long-range attractive forces, such as van der Waals interactions, and short-range repulsion, that can be steric hindrance or electrostatic for instance. In the case of metallic nanoparticles, the colloidal stability is usually not obtained with the bare metal but by capping the particles with an organic layer that may play several roles at the nucleation, growth or colloidal stages: catalytic reduction of precursor salts, passivation against oxidation, electrostatic or amphiphilic stabilization. In particular, gold colloid can be obtained by the reduction of Au(III) salts in the presence of citrate trisodium, in which crystalline gold nuclei are generated all at once, grow simultaneously and end up as mono-disperse citrate-capped colloids stabilized by anionic repulsion. Self-assembling the nanoparticles into higher order architectures therefore consists of slightly reducing the stabilization conditions to favor a predominantly attractive rather than a net repulsive interaction. One intuitive strategy consists of screening off the repulsion potential to promote the attractive interactions. Turkevitch demonstrated this by adding NaClO<sub>4</sub> solutions to citrate-stabilized 20 nm diameter gold colloids (Enüstün and Turkevich 1963). The formation kinetics and morphology of the resulting aggregates depend on the stabilizing potential (citrate concentration) and the ionic strength (perchlorate concentration). Interestingly, when both these parameters are simultaneously low, 1D ('fibrous') aggregation is observed although no clear mechanism is found at the time. Similar self-assembled structures are observed when citrates are partially neutralized, rather than screened, by adding a strong acid. In a more recent series of experiments by Kotov and colleagues, semiconducting CdTe colloids stabilized by citrate anions were self-assembled by washing away part of the citrate layer with water (Tang *et al* 2002). Upon reducing the electrostatic repulsion, the nanoparticle interaction is dominated by the attractive potential due to permanent electrical dipoles borne by each crystalline nanoparticle. The symmetry of the obtained superstructures is governed by the axisymmetry of the dipolar interaction: nanoparticle chains and chain networks are observed. A more rational approach to nanoparticle self-assembly consists in replacing the stabilizing layer by an encoded layer that will maintain the nanoparticle integrity and the colloidal stability while triggering the self-assembly process. A striking example is the replacement of citrates by thiol-terminated single strand oligonucleotides, which allow the thermally reversible association of double strand DNA that assembles the nanoparticles into large 3D networks (Alivisatos *et al* 1996, Mirkin *et al* 1996). The LSP borne by the nanoparticles are thus brought into close proximity and the coupling results in a spectral red-shift (typically from 520 to about 600 nm) and reduction of the plasmon band. This plasmonic phenomenon associated with the unique sensitivity of DNA pairing to single base pair mismatch is a sensitive biosensing method, which is probably among the first applications of bottom-up nanoplasmonics (Mirkin *et al* 2007). Unlike the dipolar interaction of semi-conducting nanoparticles, DNA-pairing of metallic colloids can only generate isotropic assembly and the resulting particle networks are compact. One option to break the symmetry of the resulting network is to replace isometric nanoparticles by nanorods. Chains of gold nanorods were obtained by controlling the topospecificity of the ligand exchange (Thomas *et al* 2004). End-to-end nanorod self-assembly was obtained by taking advantage of the moderate affinity of the stabilizing surfactant layer (cetyltrimethylammonium bromide (CTAB)) for the [111] crystallographic faces constituting the rod tips compared to the higher affinity of CTAB for the [100] side faces (Johnson *et al* 2002). This allowed the specific entry of hydrogen-bond forming moieties (mercaptopropionic acid, MPA, or mercaptioundecanoic acid, MUA) at the nanorod

ends thus resulting in the purely linear cross-linking of nanorods. The spatial segregation of chemical groups on the surface of crystalline colloids is a crucial step in self-assembling particle networks and it was recently applied to isometric nanoparticles. Since isometric gold nanoparticles are actually penta-twinned decahedra, a careful balance between two capping ligands results in the spatial partition of the two kinds of capping molecules (Jackson *et al* 2004). Moreover, by varying the molar ratio of the ligands, the self-assembled mixed ligand monolayer undergoes a phase diagram-like evolution with the formation of ordered ring structures composed of one or the other ligand. In such highly curved molecular monolayer patterns, the two polar singularities have subsequently been targeted and grafted with a single MUA ligand which is an elegant approach to forming linear chains of typically 10–20 isometric nanoparticles by interparticle amidation with 1,6-diaminohexane (Devries *et al* 2007). Through the previous examples, one realizes that network complexity and interconnectivity, on one hand, and programmed self-assembly on the other hand, have not yet converged to an efficient protocol able to produce extended networks of metallic nanoparticles positioned closely enough to promote a strong coupling of the individual localized plasmons. Kotov's work on CdTe nanoparticle chain networks remains topologically the closest structure that one would wish for complex PNNs, yet, metallic particles do not bear any permanent electrical dipole to initiate and propagate the chain formation. We have recently showed that replacing, rather than washing away, part of the capping citrate monolayer by neutral mercaptoethanol (MEA), which forms self-assembled monolayers specifically on [111] crystalline planes of gold, resulted in citrate and MEA ligands segregation, which in turn produced an anisotropic anionic charge distribution that can be assimilated to a net surface charge dipole (Lin *et al* 2005). The induced surface dipole borne by each particle interacts with its neighbor in a similar way to the permanent electrical dipoles in Kotov's system and extended networks of gold nanoparticle chains of similar morphology are thus obtained. The networks are composed of single particle chains that typically comprise up to 20 nanoparticles between two branching points. The onset of the network formation corresponds to an Au : MEA molar ratio of 1 : 1500 which corresponds to MEA coverage of 58% for 13 nm diameter gold nanoparticles. The network self-assembly process is rather slow (typically 2–3 days) as one would expect from a dipolar mechanism which is triggered only after enough maturation of the self-assembly of hydrogen bond-stabilized MEA monolayers on the [111] planes has occurred. Colloidal suspensions of networks are stable for several weeks at room temperature, are not destroyed by elevated temperatures but do not sustain ultrasonication. The optical signature of the formation of these PNNs is the slight shift-less decrease of the 520 nm band and the emergence of a large and intense band, which stabilizes at about 700 nm as illustrated in figure 1. As will be detailed in section 3.2, this second band has been shown to result from the strong coupling between plasmon modes localized on individual nanoparticles and separated from its nearest neighbor by about 1 nm (Girard and Dujardin 2006, Girard *et al* 2006, Lin *et al* 2005). Noticeably, when MEA is in very large excess, PNNs are replaced by compact isotropic aggregates, the optical signature of which is a single broad feature centered at about 580–600 nm perfectly reminiscent of the DNA-driven compact aggregates.

Regardless of the preparation method or the resulting morphologies, should self-assembled nanoparticle chains and PNNs be integrated into plasmonic devices, post-processing will be required to deposit the fragile superstructures onto a substrate and subsequently interface them in such a way that they can be addressed with a laser spot. The following subsection provides some options currently being explored to implement this next technological step.

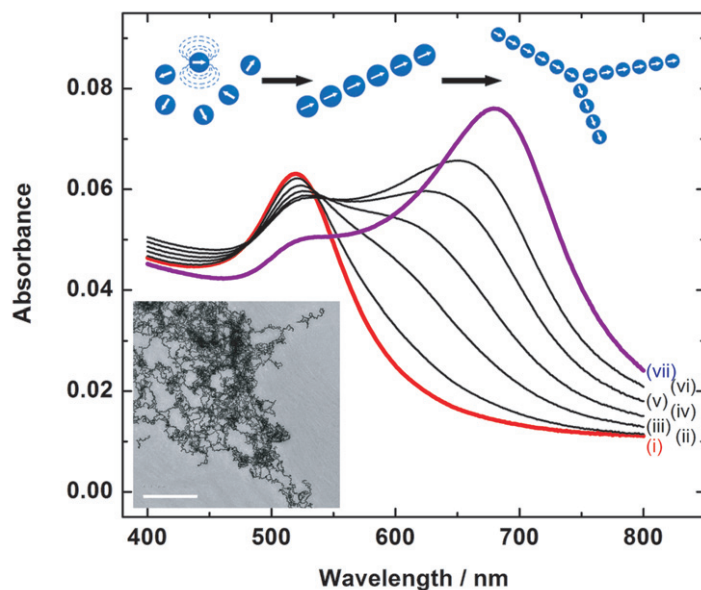


**Figure 1.** Formation of plasmonic particle networks from colloidal gold. Isolated 13 nm diameter gold nanocrystals are self-assembled by addition of MEA. The self-assembly into chains and then branched networks by induced dipolar interactions (scheme in upper insert) is followed in time by UV-visible spectrophotometry, which shows the decrease of the 520 nm band as the 700 nm band emerges. After 24–48 h, the networks are fully formed and can be observed in transmission electron microscopy (image in lower insert, bar 500 nm). Spectra are taken at (i) 0 min, (ii) 30 min, (iii) 1 h, (iv) 1.5 h, (v) 2 h, (vi) 2.5 h and (vii) 24 h after addition of MEA.

## 2.2. Deposition on dielectric surfaces

The transfer of colloidal particles from a suspension onto a solid substrate has been a major challenge in recent years, if only for its importance in photonics for example in the fabrication of photonic bandgap devices by depositing a few layers of colloidal photonic crystal (Vlasov *et al* 2001) or in using deposited colloids as masks for shadow evaporation (‘nanosphere lithography’) of plasmonic metal nanostructures (Haynes and Duyne 2001). The deposition of sub-100 nm colloidal metallic nanoparticles into substrate-bound nanopatterns has been reported for site-specific catalysis purposes (Golovko *et al* 2005) or as a tagging method for revealing biomolecular interactions (Lee *et al* 2004). However, few attempts for producing nanoparticle chains or networks by the direct deposition of colloidal nanoparticles have been reported. One surprisingly simple method consists of assembling parallel 1D lines of single particle width by pulling a substrate through a dilute Langmuir–Blodgett particle monolayer with a stick–slip motion of the water–substrate contact line. The lines are deposited perpendicularly to the substrate motion direction (Huang *et al* 2006). Desired nanoparticle aggregate deposition can also be achieved by nanostructuring the host substrate and driving the nanoparticle movement by capillary forces (Gordon and Peyrade 2006). While these techniques have demonstrated (or can straightforwardly be generalized to) line formation, the particle spacing within the lines, a crucial parameter which determines the localized plasmon coupling,

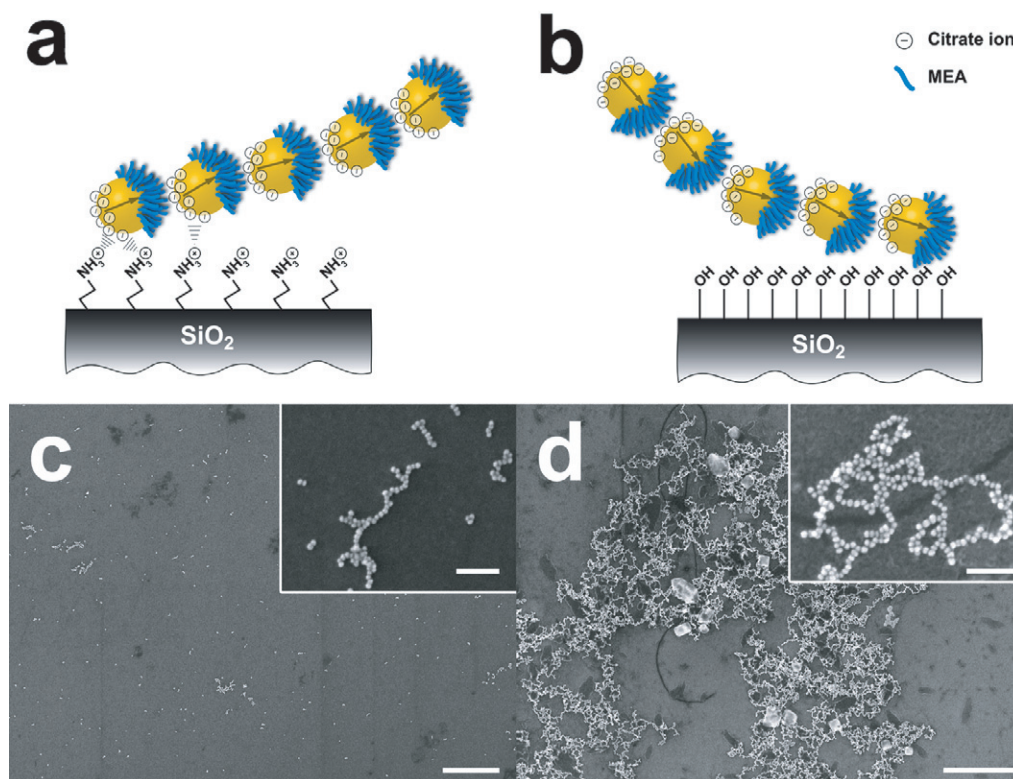


**Figure 2.** (a) Schematic view of the electrostatically driven adsorption of nanoparticle chains onto an aminopropyltriethoxysilane (APTES)-treated substrate by attractive interaction between citrate and ammonium ions. (b) Corresponding view of the adsorption of PNN onto freshly oxidized silica substrate by hydrogen-bond interaction between MEA and surface silanol. (c) Large-scale (main) and zoom (insert) scanning electron microscopy (SEM) images of fragmented PNN on APTES-functionalized substrates. Main and insert scale bars are 1.0  $\mu\text{m}$  and 100 nm, respectively. (d) Large-scale (main) and zoom (insert) SEM images of intact and well-spread PNN on freshly cleaned silica substrates. Main and insert scale bars are 1.0  $\mu\text{m}$  and 100 nm, respectively.

is somewhat adjustable but not satisfactorily controlled. Moreover, complex 2D network architecture would be difficult to implement by either of these methods. In our case, complex networks are spontaneously formed and the interparticle distance is intrinsically determined by the mixed citrate/MEA capping layer and has been observed to be both very small (1 nm) and uniform enough ( $\text{SD} < 20\%$ ) to yield a good coupling efficiency. However, the controlled deposition, spreading and addressing of the colloidal superstructure is the corresponding challenge. Since the nanoparticle chains are stabilized by citrate and MEA, two approaches have been envisioned as schematically illustrated in figure 2. The exposed  $-\text{OH}$  ends of the nanoparticle-borne MEA can bind to  $\text{Si}-\text{OH}$  rich surfaces by hydrogen bonds (figure 2(b)). Moreover, the residual anionic citrate molecules on the PNN particles interact favorably with cationic substrates by electrostatic interactions. For this, glass surfaces functionalized with aminopropyltriethoxysilane (APTES) monolayers, which exhibit a cationic ammonium surface at neutral pH (figure 2(a)), have been prepared by gas phase reaction (Bonell *et al* 2008).

Nanoparticle chain networks pre-formed in solution have been deposited, typically 24 or 48 h after formation, on either of these two types of surface by spin-coating at 5000 rpm speed and for 180 s dwell time. Interestingly, suspensions spin-coated onto APTES-functionalized substrates yielded a uniform deposition of small chain fragments, particle clusters or even isolated gold colloids (figure 2(c)). Such fragmentation was not observed when the suspensions were deposited on carbon films supported on transmission electron microscope (TEM) grids, which instead presented intact PNN. On amino functionalized substrates, PNN are adsorbed through ammonium/citrate electrostatic interactions, which are much stronger than the intra-chain dipolar cohesion force, as depicted schematically in figure 2(a). Fragmentation of PNNs can result from mechanical tearing of the PNN during spinning or by the passage of the receding liquid meniscus upon final drying. In contrast, when the PNN suspensions were spin-coated onto freshly cleaned, non-functionalized silica surfaces, SEM observations showed intact branched networks with morphologies very similar to those observed on carbon films by TEM (figure 2(d)). The absence of clumping or vertical stacking confirms that single chain networks are present in the suspension and that the adsorption interaction is strong enough to obviate the clustering by a receding water meniscus upon drying. Here, the hydrogen-bonding between each accessible MEA molecule and the substrate is weak enough compared to the intra-chain dipolar cohesion force to avoid the disruption of the self-assembly but, when repeated simultaneously a large number of times, strong enough to induce the PNN chemisorption onto the silica substrates (figure 2(b)). These two extreme cases illustrate how the nature and intensity of the PNN/substrate interaction can be tuned to simultaneously promote sufficient interaction to efficiently adsorb the networks onto technologically relevant substrates but avoid PNN disassembly upon adsorption and drying. Details on the location and addressing of deposited PNN are described elsewhere (Bonell *et al* 2008). This promising approach is being refined to get complete control for future plasmonic interfacing of the PNN as well as the investigation of their near-field optical properties.

### 3. Near-field optical properties of self-assembled plasmonics

In *bottom-up* plasmonics we have to consider the description of complex low-symmetry systems. The size of the building blocks that compose these structures can be of the order of or much smaller than the incident wavelength. Additionally, the nanostructures turn out to be more or less coupled with the microscale surroundings and quantum effects should be properly treated in the ultimate regime where active molecules are coupled with the nanostructures. In order to treat these composite systems, two different scales will be considered in the following sections with two relevant theoretical methods.

#### 3.1. A GDM for the submicrometre scale

Under the influence of an arbitrary electromagnetic field characterized by the vector couple  $\{\mathbf{E}_0(\mathbf{r}, t); \mathbf{H}_0(\mathbf{r}, t)\}$ , the local electric field  $\mathbf{E}(\mathbf{r}, t)$  inside and around a plasmonic system composed of  $N_p$  similar or different building blocks (see example given in figure 3) is dramatically modified. In fact the new time-dependent field  $\mathbf{E}(\mathbf{r}, t)$  can be obtained by solving a Lippmann–Schwinger equation

$$\mathbf{E}(\mathbf{r}, \omega) = \mathbf{E}_0(\mathbf{r}, \omega) + \frac{1}{4\pi} \sum_{p=1}^N \int_{V_p} (\epsilon_p(\omega) - \epsilon_{\text{env}}(\omega)) \mathbf{S}(\mathbf{r}, \mathbf{r}', \omega) \cdot \mathbf{E}(\mathbf{r}', \omega) \, d\mathbf{r}' \quad (1)$$

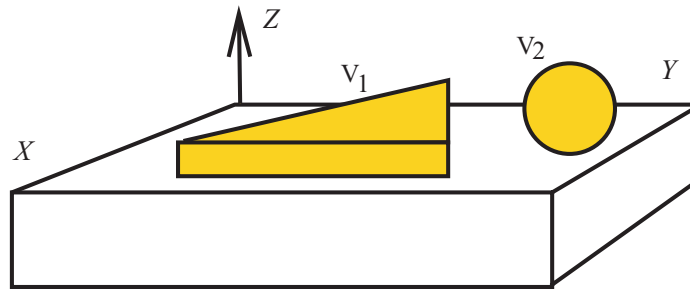


**Figure 3.** Schematic drawing of two gold colloidal particles deposited on a dielectric substrate.

written from the *time Fourier transforms*  $\mathbf{E}_0(\mathbf{r}, \omega)$  and  $\mathbf{E}(\mathbf{r}, \omega)$  of the applied and local fields, respectively (CGS units). In this integral equation,  $\epsilon_p(\omega)$  and  $\epsilon_{\text{env}}(\omega)$  represent the permittivity of the  $p$ th metallic particles and the surrounding medium, respectively. The response function  $\mathbf{S}(\mathbf{r}, \mathbf{r}', \omega)$  is the Green dyadic tensor associated with the bare dielectric surface (i.e. computed in the absence of any metallic particles). This quantity, also called the field propagator, must match the boundary conditions on the plane surface. One has then

$$\mathbf{S}(\mathbf{r}, \mathbf{r}', \omega) = \mathbf{S}_0(\mathbf{r}, \mathbf{r}', \omega) + \mathbf{S}_{\text{surf}}(\mathbf{r}, \mathbf{r}', \omega), \quad (2)$$

where  $\mathbf{S}_0(\mathbf{r}, \mathbf{r}', \omega)$  represents the Green dyadic response function of the homogeneous medium (permittivity  $\epsilon_{\text{env}}(\omega)$ ), and  $\mathbf{S}_{\text{surf}}(\mathbf{r}, \mathbf{r}', \omega)$  takes into account the presence of the dielectric surface that supports the plasmonic components. In the numerical work to be discussed in this paper, the retarded propagators  $\mathbf{S}_0(\mathbf{r}, \mathbf{r}', \omega)$  and  $\mathbf{S}_{\text{surf}}(\mathbf{r}, \mathbf{r}', \omega)$  have been chosen in the reference (Girard 2005), and for the dielectric constant of the metal we have used the experimental data of Palik (1998). Generally, the use of these experimental data in plasmonics gives reliable results (i.e. in good agreement with experiment) for particle size greater about 10 nm. Below this size, other effects should be accounted for (additional dissipation and spatial dispersion effects) by adopting more fundamental description of their optical electronic response.

Another important point should be mentioned. Beside this method dedicated to near-field optics in dielectric and metallic nanostructures, we find also many other approaches that combines different concepts (Baida and Van Labeke 2003, Baida *et al* 2003, Jin and Xu 2004, Maier *et al* 2003a, Novotny 1996, Porto *et al* 1999). Particularly, the finite difference time domain (FDTD) schemes was successfully applied to different near-field optical problems (Baida and Van Labeke 2003, Baida *et al* 2003, 2004, Christensen 1995, Jin and Xu 2004, Maier *et al* 2003a, Tanaka *et al* 2001). Nevertheless, due to the time domain discretization, dispersive materials such as metals are difficult to handle with FDTD. In particular, experimental dispersion curves cannot directly be incorporated in this scheme, whereas they can easily be accounted for in the frequency domain technique described in this section.

**3.1.1. Near-field optical response.** In almost realistic situations, searching for exact solutions of (1) needs a volume discretization procedure of the source region occupied by the plasmonic particles. Generally each particle volume  $V_p$  is discretized with  $n_p$  identical elementary volumes

$v_p$ . Such a procedure converts integrals into discrete summations:

$$\mathbf{E}(\mathbf{r}, \omega) = \mathbf{E}_0(\mathbf{r}, \omega) + \sum_{p=1}^N \eta_p(\omega) \sum_{j=1}^{n_p} [\mathbf{S}_0(\mathbf{r}, \mathbf{r}_{p,j}, \omega) + \mathbf{S}_{\text{surf}}(\mathbf{r}, \mathbf{r}_{p,j}, \omega)] \cdot \mathbf{E}(\mathbf{r}_{p,j}, \omega). \quad (3)$$

In this expression, the parameters  $\eta_p(\omega)$  are homogeneous to dipolar polarizabilities:

$$\eta_p(\omega) = \frac{\epsilon_p(\omega) - \epsilon_{\text{env}}(\omega)}{4\pi} v_p, \quad (4)$$

and the vector  $\mathbf{r}_{p,j}$  represents the location of the  $j$ th discretized cells inside the  $p$ th metallic particle. In a first step, we look for the self-consistent electric field inside the metal particles. This procedure leads to a system of  $N \times n_p$  vectorial equations with  $N \times n_p$  unknown fields  $\mathbf{E}(\mathbf{r}_{p,j}, \omega)$ :

$$\mathbf{E}(\mathbf{r}_{q,i}, \omega) = \mathbf{E}_0(\mathbf{r}_{q,i}, \omega) + \sum_{p=1}^N \eta_p(\omega) \sum_{j=1}^{n_p} [\mathbf{S}_0(\mathbf{r}_{q,i}, \mathbf{r}_{p,j}, \omega) + \mathbf{S}_{\text{surf}}(\mathbf{r}_{q,i}, \mathbf{r}_{p,j}, \omega)] \cdot \mathbf{E}(\mathbf{r}_{p,j}, \omega), \quad (5)$$

where the indexes  $i$  and  $j$  vary from 1 to  $n_p$  and the indexes  $q$  and  $p$  label the metal particles. In a given particle  $p$ , when the index  $i = j$ , the Green dyadic function  $\mathbf{S}_0(\mathbf{r}_{q,i}, \mathbf{r}_{q,i}, \omega)$  exhibits a mathematical singularity. This divergence that occurs inside the source region, can be easily removed by applying the following procedure:

1. First, we use the symmetry properties of the homogeneous propagator  $\mathbf{S}_0$ . That leads to:

$$\mathbf{S}_0(\mathbf{r}_{q,i}, \mathbf{r}_{q,i}, \omega) = \mathbf{I} C_p(\omega), \quad (6)$$

where  $\mathbf{I}$  labels the identity tensor and  $C_p(\omega)$  is a frequency dependent coefficient that will be determined in the following step.

2. Let us consider a single discretized cell located at the position  $\mathbf{r}_{q,i}$  inside a homogeneous surroundings. In this case, equation (5) reduces to:

$$\mathbf{E}(\mathbf{r}_{q,i}, \omega) = \mathbf{E}_0(\mathbf{r}_{q,i}, \omega) + \eta_p(\omega) \mathbf{S}_0(\mathbf{r}_{q,i}, \mathbf{r}_{q,i}, \omega) \cdot \mathbf{E}(\mathbf{r}_{q,i}, \omega). \quad (7)$$

Now by using equation (6) one may write the following vectorial equation:

$$\mathbf{E}(\mathbf{r}_{q,i}, \omega) [1 - \eta_p(\omega) C_p(\omega)] = \mathbf{E}_0(\mathbf{r}_{q,i}, \omega), \quad (8)$$

from which the normalization coefficient  $C_p(\omega)$  associated with the  $p$ th particle can be expressed from the ratio  $\mathcal{R}_p(\omega) = E_0(\mathbf{r}_{q,i}, \omega) / E(\mathbf{r}_{q,i}, \omega)$  between applied field amplitude and local field amplitude inside the cell:

$$C_p(\omega) = (1 - \mathcal{R}_p(\omega)) \frac{1}{\eta_p(\omega)}. \quad (9)$$

Finally, by introducing the usual local field factor:

$$\mathcal{R}_p(\omega) = \frac{\epsilon_p(\omega) + 2\epsilon_{\text{env}}(\omega)}{3\epsilon_{\text{env}}}, \quad (10)$$

one obtains:

$$C_p(\omega) = -\frac{4\pi}{3\epsilon_{\text{env}}(\omega) v_p}. \quad (11)$$

**Table 1.** Analytical expressions of  $\eta_p(\omega)$  and  $C_p(\omega)$  for two different meshings of the plasmonic particles.  $b$  represents the distance between two consecutive cells.

Meshing	Cell volume	$\eta_p(\omega)$ coefficient	$C_p(\omega)$ coefficient
Meshing	Cell volume	$\eta_p(\omega)$ coefficient	$C_p(\omega)$ coefficient
Cubic	$b^3$	$\frac{\epsilon_p(\omega) - \epsilon_{\text{env}}(\omega)}{4\pi} b^3$	$-\frac{4\pi}{3\epsilon_{\text{env}}(\omega)b^3}$
Hexagonal compact	$b^3/\sqrt{2}$	$\frac{\epsilon_p(\omega) - \epsilon_{\text{env}}(\omega)}{4\sqrt{2}\pi} b^3$	$-\frac{4\sqrt{2}\pi}{3\epsilon_{\text{env}}(\omega)b^3}$

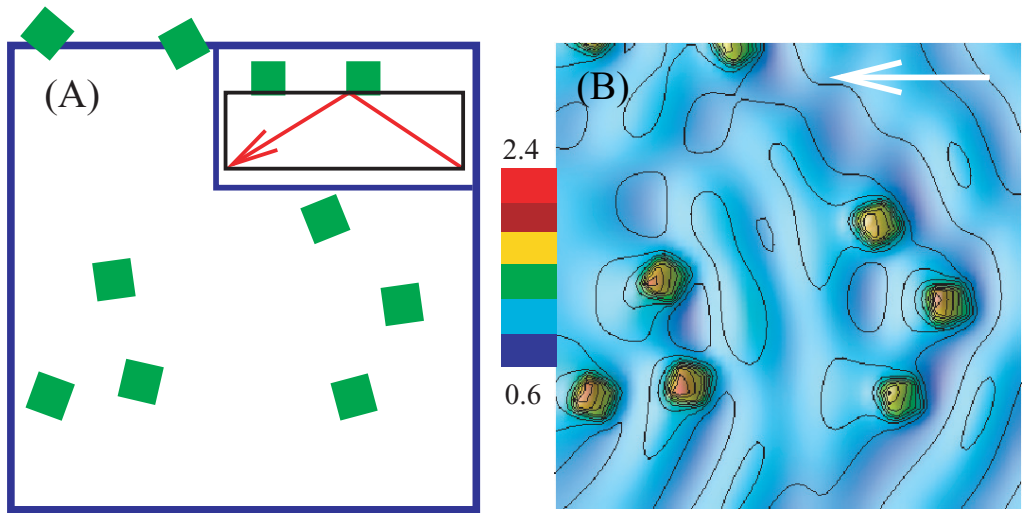


**Figure 4.** Example of computation of optical near-field intensity in the vicinity of cubic colloidal gold particles of 100 nm in side (color scale increasing from blue to red). The particles deposited on a plane silica surface are surrounded by water (optical index 1.33). The surface of water–silica interface is illuminated by total internal reflection at the incident wavelength  $\lambda_0 = 700$  nm: (A) top view of eight cubic gold particles deposited on the sample; (B) electric field intensity map computed in the transverse magnetic (TM) polarization mode in a plane located at 15 nm from the top of the gold cubes (window size  $1500 \times 1500$  nm<sup>2</sup>).

For a given metal particle (labeled by the subscript  $p$ ), these developments indicate that the solving procedure mainly relies on the knowledge of the two parameters  $\eta_p(\omega)$  and  $C_p(\omega)$ . In fact, they are directly related to the discretization volume  $v_p$  that itself depends on the discretization grid used to mesh the particles. In table 1, we have gathered the expressions of these coefficients for both *cubic* and *hexagonal compact* discretization grids.

From the analytical expressions of  $\eta_p(\omega)$  and  $C_p(\omega)$ , we can numerically solve the set of equations (5) and thus obtain the complete self-consistent field distribution  $\mathbf{E}(\mathbf{r}_{q,i}, \omega)$  inside the metal particles. From these data, the electric field outside the particles can be computed by applying equation (3). In figures 4 and 5, we present several simulations of optical near-field intensity in the vicinity of cubic colloidal gold particles deposited on a transparent

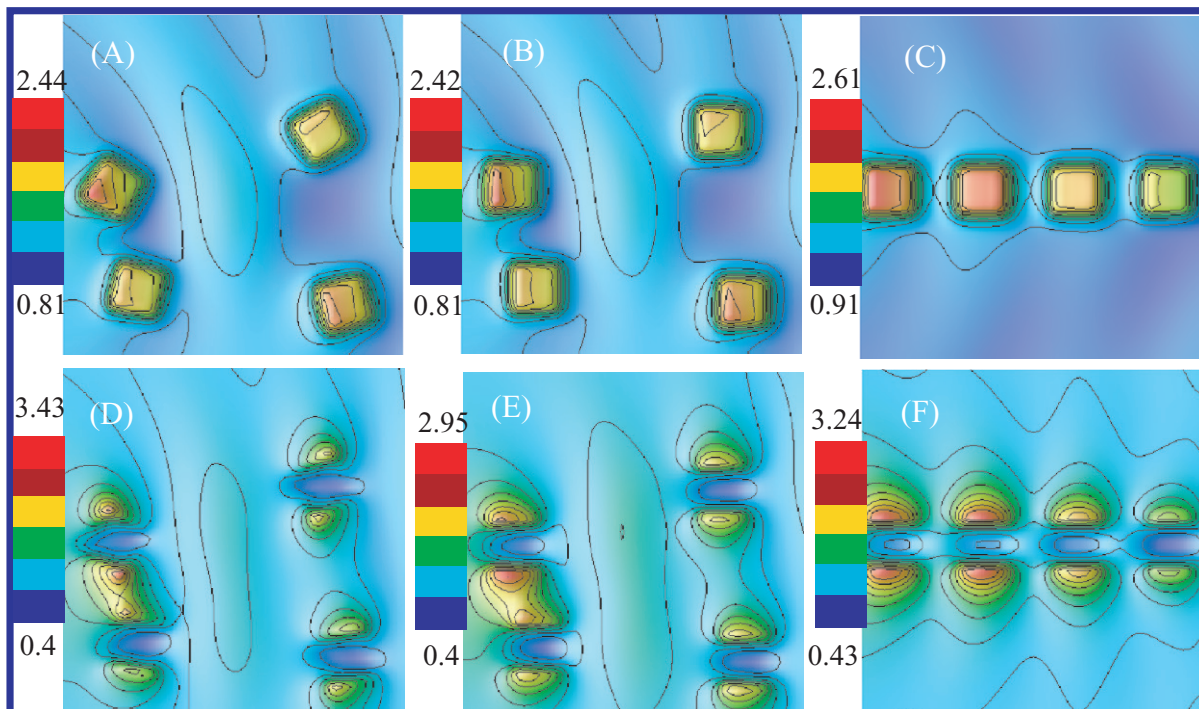


**Figure 5.** Sequence of optical near-field images describing the evolution of near-field patterns when passing from disordered to ordered structures arranged to form a linear chain (color scale increasing from blue to red, window size  $750 \times 750 \text{ nm}^2$ ). (A), (B) and (C) TM polarization mode; (D), (E) and (F) transverse electric (TE) polarization mode. All optical and geometrical parameters are identical to those of figure 4.

substrate. In figure 4, the simulation sequence begins with randomly located and oriented cubic particles excited by a quasi 2D surface evanescent wave generated by total internal reflection. In figure 4(B), the white arrow indicates the propagation direction of this surface wave. When the sample is illuminated under TM polarization the metal cubes emerge from a smooth but complex interference pattern with a positive contrast. We notice that the disordered arrangement of the particles tends to downgrade the image–object relation. In figure 5, we analyze the changes of the near-field intensity maps when gradually increasing the symmetry of the cube arrangement to end with a linear chain. We show a zoom of the central part of figure 4, where the near-field tends to symmetrically confine along the chain under TM and TE polarization (cf figures 5(C) and (F)). Such plasmonic chains can be used to convey optical signal at visible wavelengths (Maier *et al* 2001). More specifically, the near-field optical transmittance of similar structures has been addressed (Girard and Quidant 2004) in both the addressing modes.

*3.1.2. Spectroscopic properties and local density of photonic states.* For such metallic objects, the excitation wavelength  $\lambda_0$  is an important parameter. The excitation of surface plasmons causes a characteristic field enhancement compared to the incident electromagnetic wave.

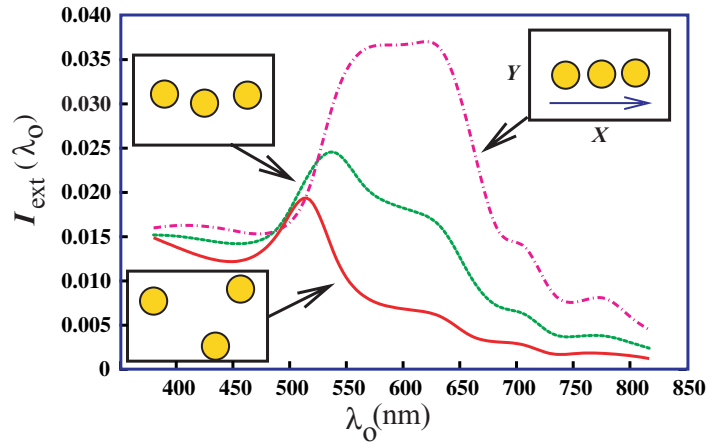


**Figure 6.** Evolution of the extinction spectra of three spherical colloidal gold particles when passing from a disordered to an ordered linear structure. The particles, in air, are adsorbed on a glass planar substrate. The excitation electric field is polarized along the  $OY$ -axis (see blue arrow in the right frame). Each curve is associated with the corresponding geometry.

Different physical quantities can be used to characterize the spectroscopic properties of a self-assembled plasmonic system:

1. The near-field optical spectra  $I_{\text{nf}}(\mathbf{R}, \lambda_0)$  that will give the variation of the optical near-field intensity recorded at a given location  $\mathbf{R}$  above the sample versus the incident wavelength ( $\lambda_0$ ). Actually, the photon scanning tunneling microscope (PSTM) appears to be the ideal instrument to measure such local spectra because such a device delivers signals proportional the electric near-field intensity. This signal can be computed from the electric field given by equation (4) at the position  $\mathbf{r} = \mathbf{R}$ .
2. Far-field extinction spectra. Specifically designed plasmonic nanostructures can also be characterized by their far-field extinction spectra  $I_{\text{ext}}(\lambda_0)$  (with  $\lambda_0 = 2\pi c / \sqrt{\epsilon_{\text{env}}}\omega$ ). This quantity usually called *extinction cross-section* is commonly recorded with spectrometers located in the far-field zone around the sample. Its mathematical description involves the knowledge of the electric polarization  $\mathcal{P}(\mathbf{r}, \lambda_0)$  inside the materials. For example, inside the  $i$ th cell of the  $p$ th building block of a self-assembled plasmonic system, we can write:

$$\mathcal{P}(\mathbf{r}_{i,p}, \lambda_0) = \eta_p(\lambda_0)\mathbf{E}(\mathbf{r}_{p,i}, \lambda_0) \quad (12)$$

that will be used to form the far-field extinction spectrum:

$$I_{\text{ext}}(\lambda_0) = \frac{8\pi^2}{\lambda_0 |E_0|^2} \sum_{p=1}^N \sum_{i=1}^{n_p} \Im(\mathbf{E}_0^*(\mathbf{r}_{p,i}, \lambda_0) \cdot \mathcal{P}(\mathbf{r}_{i,p}, \lambda_0)). \quad (13)$$

An example of simulation of this law is provided in figure 6, where three identical spherical gold particles (80 nm in diameter) are discretized with 373 cells located at the nodes at a hexagonal compact array ( $N = 3$ ;  $n_1 = n_2 = n_3 = 373$ ). In agreement with previous results, the simulated spectra showed a progressive disappearance of the intensity of the usual transverse 520 nm peak as well as the appearance of a longitudinal plasmon band of increasing intensity which is shifted to lower energy when lining up the metal particles,

in qualitative agreement with figure 1 (more adequate calculation are presented in Lin *et al* (2005) and Girard and Dujardin (2006).

3. Local density of states (LDOS) spectra. Precious local spectroscopic information can also be extracted from the LDOS spectra. Generally, material particles in the free space modifies the LDOS of electrons (Tersoff and Hamann 1985), photons (Agarwal 1975) and other elementary excitations. This LDOS change is usually compared to the free space value.

In optics, the role of the LDOS—also called *local mode density*—is well identified in the decay rate process of fluorescent molecules. This quantity also appears as a constant factor in Planck's law of blackbody radiation (Landau and Lifshitz 1960, Loudon 2000). In a perfectly homogeneous medium which sustains only radiative modes, the three usual Cartesian directions are equivalent so that this factor  $\rho(\mathbf{r}, \omega)$  appears as a sum of three equivalent quantities  $\rho_\alpha(\mathbf{r}, \omega)$  (with  $\alpha = x, y$  or  $z$ ) that represent *the three polarized* LDOS (also called partial LDOS). This property is no longer satisfied in the presence of a corrugated surface or a surface supporting small particles. For instance, in the vicinity of dielectric particles adsorbed on a surface, the three polarized LDOS  $\rho_\alpha(\mathbf{r}, \omega)$  (with  $\alpha = x, y$  or  $z$ ) are dramatically modified by the presence of the evanescent modes sustained by the particles (Colas des Francs *et al* 2001). Additionally, in this case where no significant energy dissipation is expected inside the material each polarized LDOS  $\rho_\alpha(\mathbf{r}, \omega)$  is strictly proportional to the imaginary part of the Green function component  $\mathcal{S}_{\alpha,\alpha}(\mathbf{r}, \mathbf{r}', \omega)$

$$\rho_\alpha(\mathbf{r}, \omega) = \frac{1}{2\pi^2\omega} \Im[\mathcal{S}_{\alpha,\alpha}(\mathbf{r}, \mathbf{r}, \omega)]. \quad (14)$$

The detailed demonstration of this relation (14) is provided by Girard and Dujardin (2006). When dealing with plasmonic structures which generally exhibit significant dissipative properties, equation (14) does not represent *stricto sensu* the LDOS of the sample because non-radiative decay channels introduce additional contributions. Nevertheless, this relation remains valid to study the fluorescence decay rate of molecules located near plasmonic components. Actually as explained in Baffou *et al* (2008), the total decay rate  $\Gamma$  of a fluorescence level  $\omega_0$  of transition dipole  $\mu_0$  is proportional to  $\rho_\alpha(\mathbf{r}, \omega_0)$  at the location  $\mathbf{r}$  of the molecule:

$$\Gamma(\mathbf{r}) = \frac{4\pi^2\omega_0\mu_0^2}{\hbar} \rho_\alpha(\mathbf{r}, \omega_0). \quad (15)$$

This formalism is also pertinent to analyzing the EELS signal generated by fast electrons impinging a metal particle (Garcia de Abajo and Kociak 2008, Nelayah *et al* 2007). The main difficulty lies in the computation of the  $\mathcal{S}(\mathbf{r}, \mathbf{r}', \omega)$  dyadic above the sample. When dealing with *bottom-up* plasmonic nanostructures deposited on a surface, the current developments of computation methods in real space provides powerful tools to derive the electromagnetic response  $\mathcal{S}(\mathbf{r}, \mathbf{r}, \omega)$ . Indeed, the dyadic tensor can be computed by solving numerically the Dyson equation. To achieve this work, we use the discretization scheme previously introduced to solve equation (3)

$$\mathcal{S}(\mathbf{r}, \mathbf{r}', \omega) = \mathbf{S}(\mathbf{r}, \mathbf{r}', \omega) + \sum_{p=1}^N \eta_p(\omega) \sum_{j=1}^{n_p} \mathbf{S}(\mathbf{r}, \mathbf{r}_{p,j}, \omega) \cdot \mathcal{S}(\mathbf{r}_{p,j}, \mathbf{r}', \omega). \quad (16)$$

A numerical procedure to inverse Dyson's equation is detailed in Martin *et al* (1995). From the numerical data describing the spatial behavior of the imaginary part of the Green dyadic function  $\mathcal{S}(\mathbf{r}, \mathbf{r}, \omega)$ , we can model maps or LDOS spectra and partial LDOS in the vicinity of

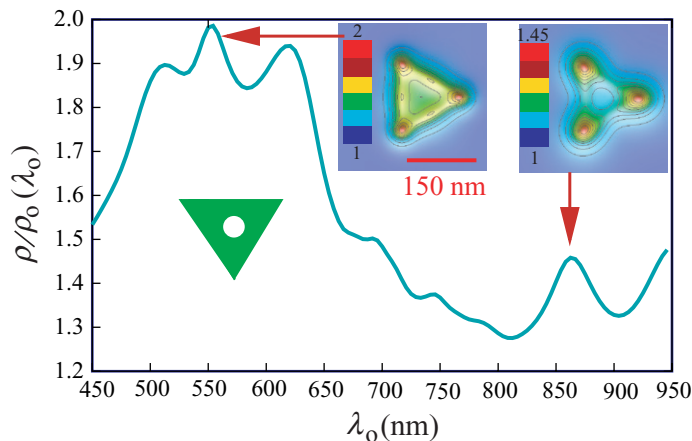


**Figure 7.** LDOS spectrum of a single gold nanoprism deposited on a glass planar surface. The spectrum is computed just above the triangle center (large white dot). The inset figures represent the corresponding LDOS maps computed in a plane located at 50 nm above the particle at the wavelengths  $\lambda_0 = 560$  nm and 850 nm, respectively. The side of the nanoprism is 150 nm and its thickness 37.5 nm.

self-assembled *bottom-up* plasmonic structures deposited on a plane surface. In figure 7, the LDOS spectrum of a single gold nanoprism is computed at 80 nm from its center. In the visible frequency range, the spectrum appears with a series of plasmon resonances beginning with the standard transverse mode occurring at  $\lambda_0 = 550$  nm. The other peaks reveal both lateral and multipolar modes associated with the structures. The subwavelength sizes of the gold particle is responsible for the high density of evanescent states localized around the nanoprism as well illustrated by the two LDOS images encapsulated in figure 7. This concentration of modes explains the high contrast observed in these two maps where the three corners of the triangle display significant enhancements. More precisely, according to the spectrum which predicts a larger LDOS intensity around  $\lambda_0 = 550$  nm than around  $\lambda_0 = 850$  nm, we observe a better confinement around the structure for the wavelength  $\lambda_0 = 550$  nm. Recently, similar symmetrical patterns have been obtained by measuring EELS amplitude maps in the vicinity of silver nanoprisms (Nelayah *et al* 2007). Additionally, as described in a recent theoretical paper by Garcia de Abajo and Kociak (2008), the concept of photonic LDOS can be successfully applied to the interpretation of the experimental EELS images.

The evolution of the LDOS intensity map is also investigated in figure 8, when two single gold nanoprisms adsorbed on the same surface are placed in close proximity. In this case, the concentric rings generated by the radiative electromagnetic modes around each particle overlap and tend to generate some hybrid *photonic states* linked to the particle couple. These simulations clearly show that either *specific self-assembling processes* or *precise nanomanipulations schemes* could be applied to the engineering of new photonic LDOS properties.

**3.1.3. Energy losses and dissipation.** In optically excited plasmonics, all energy transfer involves exchanges of photons. With traditional light sources (laser), the quantum aspect of photons is masked by the fact that the observable electromagnetic field is averaged over many

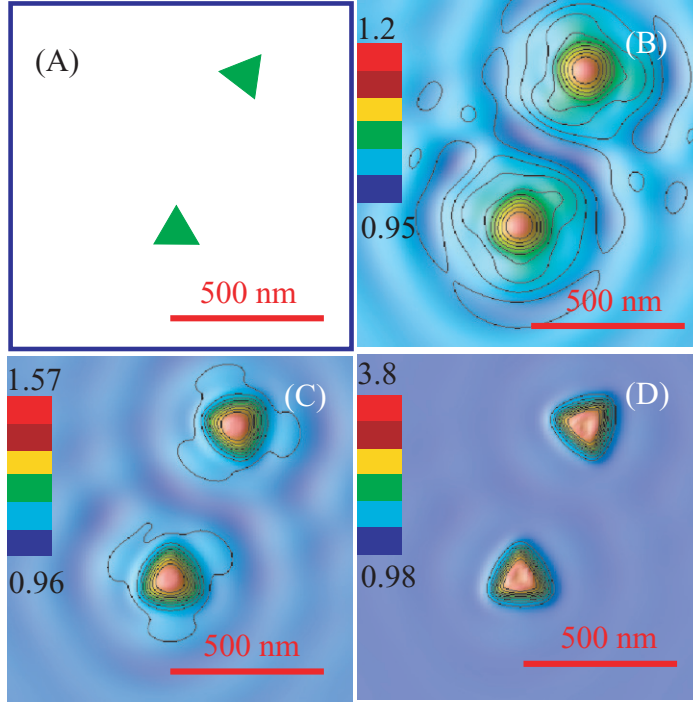


**Figure 8.** Variation of the LDOS map above two arbitrarily oriented gold nanoprisms versus the observation plane distance: (A) geometry of the glass sample supporting two triangular shaped gold particles; (B), (C) and (D) LDOS maps computed at 60, 80 and 100 nm from the glass surface, respectively.

photon states (Glauber 1963). Although, in the near-field zone, the evanescent electromagnetic field displays important imaginary wave vector components, it may be considered as a classical quantity that will enter the coupling Hamiltonian (between *electric near-field* and nanostructures) with the status of a parameter. Consequently, in plasmonics, a realistic description of such localized dissipation effects is directly related to a proper description of the imaginary parts of either the dynamical response functions of the nanostructures or the dynamical polarizabilities of molecules adsorbed on the surface sample. From the local field  $\mathbf{E}(\mathbf{r}_{q,i}, \omega)$  described by equation (5) of section 3.1.1, we can derive the amount of power dissipated by the  $i$ th elementary cell located inside the  $q$ th metallic particle. In CGS electrostatic units, this leads to:

$$Q_{q,i}(\omega) = \frac{v_q \omega \epsilon''(\omega)}{8\pi} |\mathbf{E}(\mathbf{r}_{q,i}, \omega)|^2. \quad (17)$$

This dissipated power can then be expressed in terms of the  $P_0$  power (per unit area) delivered by the illuminating laser. To achieve this transformation, we first introduce the normalized electric field intensity with respect to the illumination field intensity  $|\mathbf{E}_0(\omega)|^2$ :

$$|\overline{\mathbf{E}}(\mathbf{r}_{q,i}, \omega)|^2 = \frac{|\mathbf{E}(\mathbf{r}_{q,i}, \omega)|^2}{|\mathbf{E}_0(\omega)|^2}, \quad (18)$$

and, second, the Poynting vector relation:

$$|\mathbf{E}_0(\omega)|^2 = \frac{8\pi P_0}{c}. \quad (19)$$

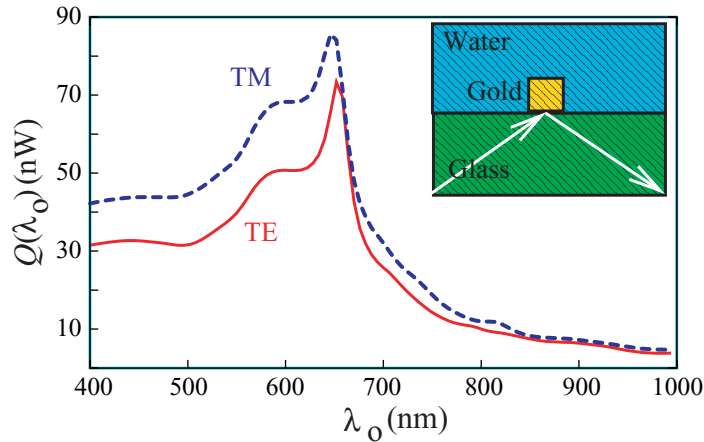


**Figure 9.** Spectra describing the heat amounts (in nanowatts) deposited by a surface evanescent wave inside a  $100 \times 100 \times 100 \text{ nm}^3$  gold cube. The two usual polarizations, TE and TM have been considered. A light beam of power  $P_0 = 100 \text{ W cm}^{-2}$  hits the glass–water interface with an incident angle  $\theta_0 = 68^\circ$ .

Finally, after applying these relations and introducing the incident wavelength  $\lambda_0$ , equation (17) reads:

$$Q_{q,i}(\lambda_0) = \frac{2\pi}{\lambda_0} v_q P_0 \epsilon''(\lambda_0) |\overline{\mathbf{E}(\mathbf{r}_{q,i}, \lambda_0)}|^2. \quad (20)$$

As described by equation (20), the heat generation rate linearly depends on the physical properties of the material. In addition, the shape of the particle plays an important role in the process efficiency. Figure 9 shows the heat dissipated by a single cubic gold particle versus the incident wavelength. The system is illuminated in a total internal reflection configuration where the two polarizations, TE and TM, have been investigated. In these two polarization states, the heat generation displays a similar plasmon resonance located in the same wavelength range. This is consistent with the cubic symmetry of the particle for which transverse and lateral plasmon modes are equivalent. Nevertheless, TM polarization appears to be more efficient than TE because of the amplitude of the glass–water transmission coefficient expected in the TM mode. The data of figure 9 is given for an incident light flux  $P_0 = 100 \text{ W cm}^{-2}$ . In this example, the heat generation rate increases by about a factor of 9 at the plasmon frequency.

### 3.2. CDA approach of the nanometre scale

At the nanometre scale, the optical properties of smaller plasmonic objects deposited on a surface (self-assembled or small individual colloidal particles) can be investigated by adapting the CDA method (Draine 1988, Draine and Flatau 1994, Doyle 1989, Purcell and Pennypacker 1973) to a planar geometry. As described in Girard (2005), near a planar dielectric surface, the mathematical writing of CDA may be compared with other volume discretization family methods based on Green dyadic functions (see previous section). Let us consider the sample depicted in figure 10. The system under study is a network of  $N$  identical subwavelength-sized nanoparticles of same radius  $a$  and dipolar polarizabilities  $\alpha(\omega)$ . When the sample is illuminated by the electric field  $\mathbf{E}_0(\mathbf{r}_i, \omega)$  associated with a surface evanescent wave generated by total

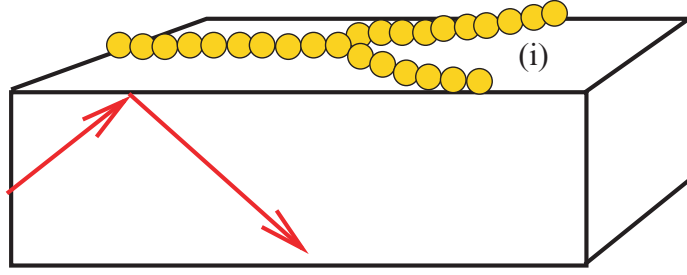


**Figure 10.** Schematic drawing of branched networks of single-nanoparticle chains deposited on a glass surface.

internal reflection, each nanometric component acquires a fluctuating dipole moment induced by the local electric field  $\mathbf{E}(\mathbf{r}_i, \omega)$

$$\mathbf{P}(\mathbf{r}_i, \omega) = \alpha(\omega) \cdot \mathbf{E}(\mathbf{r}_i, \omega) \quad (21)$$

that is self-consistently modified by the presence of the others. The many-body interactions between the nanoparticles can be introduced by writing  $N$  implicit linear equations (Hao *et al* 2004, Kelly *et al* 2003, Lazarides and Schatz 2000)

$$\mathbf{E}(\mathbf{r}_i, \omega) = \mathbf{E}_0(\mathbf{r}_i, \omega) + \sum_j \mathbf{S}(\mathbf{r}_i, \mathbf{r}_j, \omega) \cdot \alpha(\omega) \cdot \mathbf{E}(\mathbf{r}_j, \omega). \quad (22)$$

These  $N$  self-consistent equations (22) can be rewritten as a unique  $3N \times 3N$  matrix equation

$$\sum_{j=1}^N \mathbf{A}_{i,j}(\omega) \cdot \mathbf{E}(\mathbf{r}_j, \omega) = \mathbf{E}_0(\mathbf{r}_i, \omega), \quad (23)$$

with

$$\mathbf{A}_{i,j}(\omega) = \mathbf{I}\delta_{i,j} - \alpha(\omega) \cdot \mathbf{S}(\mathbf{r}_i, \mathbf{r}_j, \omega), \quad (24)$$

where  $\mathbf{I}$  is the  $3 \times 3$  identity matrix. After inversion of the linear system (24), it is possible to compute both the local fields  $\mathbf{E}(\mathbf{r}_i, \omega)$  and the electric polarization vector  $\mathbf{P}(\mathbf{r}_i, \omega) = \alpha(\omega) \cdot \mathbf{E}(\mathbf{r}_i, \omega)$  at each nanoparticle site. For spherical metallic particles, the frequency-dependent polarizability  $\alpha(\omega)$  including the *radiative correction* is given by:

$$\alpha(\omega) = \frac{\alpha_0(\omega)}{(1 - \lambda_0^3/12i\pi^3\alpha_0(\omega))} \quad (25)$$

with

$$\alpha_0(\omega) = a_i^3 \left( \frac{\epsilon_p(\omega) - \epsilon_{\text{env}}}{\epsilon_p(\omega) + 2\epsilon_{\text{env}}} \right). \quad (26)$$

**3.2.1. Field maps around self-assembled chain networks.** Within the framework of our CDA description, the electric field outside the object is merely deduced from the self-consistent field inside the metallic particles, provided that we know the field propagator  $\mathbf{S}(\mathbf{r}, \mathbf{r}', \omega)$  of the bare sample. One can write

$$\mathbf{E}(\mathbf{R}, \omega) = \mathbf{E}_0(\mathbf{R}, \omega) + \sum_j \mathbf{S}(\mathbf{R}, \mathbf{r}_j, \omega) \cdot \alpha(\omega) \cdot \mathbf{E}(\mathbf{r}_j, \omega). \quad (27)$$

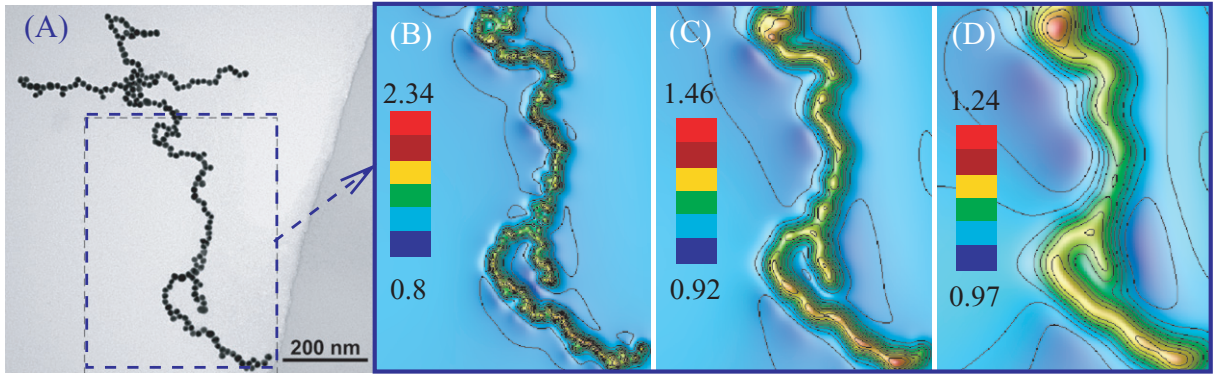


**Figure 11.** (A) TEM image showing a self-assembled Au nanoparticle chain network deposited on a substrate. (B), (C) and (D) sequence of three optical near-field intensity maps computed in three consecutive planes parallel to the sample. The plane-sample distances are 20, 30 and 50 nm, respectively.

This solution can be used to compute the normalized optical near-field intensity in the vicinity of the illuminated versus the position  $\mathbf{R}$ :

$$I(\mathbf{R}) = |\mathbf{E}(\mathbf{R}, \omega)|^2 / |\mathbf{E}_o(\mathbf{R}, \omega)|^2. \quad (28)$$

From this relation, we have simulated a sequence of three near-field optical maps of a PNN deposited on a transparent surface (cf figure 11). In the total internal illumination configuration of figure 10, the incoming light is incident with an angle of  $60^\circ$  on the sample-to-air interface. The image sequence (figures 11(B)–(D)) is computed in the p-polarized mode for resonant wavelength  $\lambda = 520$  nm (that can be identified in the extinction spectra). Three tip-to-sample distances have been successively considered. At such short approach distances, we observe a marked confinement of light around all the branches of the network with brighter regions (orange in color figures) that reveal stronger lateral coupling between the plasmonic particles. Unlike what happens with larger lithographically designed chains of gold particles (Krenn *et al* 1999a, Salerno *et al* 2005) where each gold pad generates individual bright spots in the vicinity of the particles, the optical near-field spreads out over several nanoparticle sites without significant spatial modulation. The three near-field optical image of figure 11 corresponds to short observation distances. Within this distance range, the field enhancement effect is still sufficiently efficient to reinforce the image contrast. These simulations clearly demonstrate that *chain networks self-assembled from crystalline noble metal nanoparticles* deposited on a transparent sample represent interesting objects for the subwavelength patterning of initially flat optical near-fields. The optical patterning is optimized when working at incident wavelengths close to collective plasmon modes of the network. The optical addressing of one of the chain segments could be realized by controlling the polarization state of the local near-field generated at the extremity of a SNOM tip (Maier *et al* 2003b) or by coupling with 3D spot of evanescent light (Dickson and Lyon 2000, Law *et al* 2004, Quidant *et al* 2002).

**3.2.2. LDOS in the nanometric regime.** To generalize, at the nanometre scale, the concept of photonic LDOS previously introduced in section 3.1.2, we merely have to rewrite equation (14)

$$\rho_\alpha(\mathbf{r}, \omega) = \frac{1}{2\pi^2\omega} \Im[\mathcal{S}_{\alpha,\alpha}(\mathbf{r}, \mathbf{r}, \omega)], \quad (29)$$

together with a new form of field-susceptibility  $\mathcal{S}(\mathbf{r}, \mathbf{r}', \omega)$  expressed in terms of the individual polarizabilities  $\alpha_j(\omega)$  ( $j = 1, N$ ) associated with each nanoparticle:

$$\mathcal{S}(\mathbf{r}, \mathbf{r}', \omega) = \mathbf{S}(\mathbf{r}, \mathbf{r}', \omega) + \sum_{j=1}^N \alpha_j(\omega) \mathbf{S}(\mathbf{r}, \mathbf{r}_j, \omega) \cdot \mathcal{S}(\mathbf{r}_j, \mathbf{r}', \omega). \quad (30)$$

For large  $N$  numbers of plasmonic particles, this self-consistent equation must be solved numerically (for example by applying the Dyson sequence method described in Martin *et al* (1995)). However, more tractable expressions can be obtained when considering single particles adsorbed on plane surfaces.

#### 4. Conclusion and perspective

As described in sections 2 and 3, the potential applications of self-assembled colloidal plasmonic architectures for realizing an unprecedented level of field confinement and enhanced light–matter interaction at the nanoscale open a new physics field for a mature chemistry domain. Following up along this concept, the simple fabrication of complex and extended networks of interconnected lattices of metallic nanoparticles could generate unique and unusual sub-wavelength patterning of the optical near-field. Several impacts are associated with light confinement around plasmonic structures. The most direct consequence is the improvement of the quality of the near-field optical imaging and the increased local field enhancement, and finally the light energy stocking in tiny volumes of matter. The optical physics related to the control of light confinement might also have important impact on the future solution for the miniaturization of both chemical and biological plasmonic sensors.

Finally, in terms of accumulated knowledge related to the mechanisms of light confinement, current concepts mainly rely on a description of the local dielectric constant of the material (spectra, field maps and photonic LDOS). Additional physical effects, such as non-local response, localized surface states and effects due to the limited electron mean free path can play a significant role for structures with dimensions below 10 nm. Until now, most experiments on structures are not defined enough to quantify those effects. This is of fundamental importance for the understanding of the limits that can be achieved in terms of field confinement. *Bottom-up* structures will significantly contribute in this direction with realistic applications in near-field optical research.

#### Acknowledgments

We thank Professor S Mann, Dr M Li and H Guo for fruitful discussions and a continued fruitful collaboration. This work was partially supported by the European Commission (NoE contract no. FP6-IST-2002-1-507879). In addition, we have benefited from the computing facilities provided by the massively parallel center CALMIP of Toulouse.

#### References

- Agarwal G S 1975 *Phys. Rev. A* **11** 253–64  
 Alivisatos A P, Johnsson K P, Peng X, Wilson T E, Loweth C J, Bruchez M P and Schultz P G 1996 *Nature* **382** 609–11  
 Azoulay J, Débarre A, Richard A and Tchénio P 2000 *Europhys. Lett.* **51** 374–80

- Baffou G, Girard C, Dujardin E, Colas des Francs G and Martin O J F 2008 *Phys. Rev. B* **77** 121101
- Baida F I and Van Labeke D 2003 *Phys. Rev. B* **67** 155314
- Baida F I, Van Labeke D and Pagani Y 2003 *Opt. Commun.* **225** 241–52
- Baida F I, Van Labeke D, Pagani Y, Guizal B and Al Naboulsi M 2004 *J. Microsc.* **213** 144–8
- Barnes W 1998 *J. Mod. Opt.* **45** 661–99
- Barnes W L, Dereux A and Ebbesen T W 2003 *Nature* **424** 824–30
- Bennett C R, Kirk J B and Babiker M 2001 *Phys. Rev. A* **63** 063812
- Berini P 2000 *Phys. Rev. B* **61** 10484–503
- Bonell F, Dujardin E, Li C G M, Mann S and Péchou R 2008 *J. Chem. Phys.* at press
- Bozhevolnyi S I, Erland J, Leosson K, Skovgaard P M W and Hvam J M 2001 *Phys. Rev. Lett.* **86** 3008–11
- Charbonneau R, Berini P, Berolo E and Lisicka-Shrzek E 2000 *Opt. Lett.* **25** 844–6
- Christ A, Ekinici Y, Solak H H, Gippius N A, Tikhodeev S G and Martin O J F 2007 *Phys. Rev. B* **76** 201405
- Christ A, Lévêque G, Martin O J F, Zentgraf T, Kuhl J, Bauer C, Giessen H and Tikhodeev S G 2008 *J. Microsc.* **229** 344–53
- Christensen D A 1995 *Ultramicroscopy* **57** 189–95
- Colas des Francs G, Girard C and Martin O J F 2003 *Phys. Rev. A* **67** 053805
- Colas des Francs G, Girard C, Weeber J, Chicane C, Weeber J, Dereux A and Peyrade D 2001 *Phys. Rev. Lett.* **86** 4950–3
- Das P and Metiu H 1982 *J. Phys. Chem.* **89** 4680–7
- Devaux E, Ebbesen T W, Weeber J C and Dereux A 2003 *Appl. Phys. Lett.* **83** 4936–8
- Devries G A, Brunnbauer M, Hu Y, Jackson A M, Long B, Neltner B T, Uzun O, Wunsch B H and Stellacci F 2007 *Science* **315** 358–61
- Dickson R M and Lyon L A 2000 *J. Phys. Chem. B* **104** 6095–98
- Doyle W T 1989 *Phys. Rev. B* **39** 9852–8
- Draine B T 1988 *Astrophys. J.* **333** 848–72
- Draine B T and Flatau P J 1994 *J. Opt. Soc. Am. A* **11** 1491–9
- Enüstün B V and Turkevich J 1963 *J. Am. Chem. Soc.* **85** 3317–28
- Félidj N, Aubard J, Lévi G, Krenn J R, Salerno M, Schider G, Lamprecht B, Leitner A and Aussenegg F R 2002 *Phys. Rev. B* **65** 075419
- Frey H G, Witt S, Felderer K and Guckenberger R 2004 *Phys. Rev. Lett.* **93** 200801
- Garcia de Abajo F J and Kociak M 2008 *Phys. Rev. Lett.* **100** 106804
- Gerton J M, Wade L A, Lessard G A, Ma Z and Quake S R 2004 *Phys. Rev. Lett.* **93** 180801
- Girard C 2005 *Rep. Prog. Phys.* **68** 1883–933
- Girard C and Dujardin E 2006 *J. Opt. A: Pure Appl. Opt.* **8** S73–86
- Girard C, Dujardin E, Li M and Mann S 2006 *Phys. Rev. Lett.* **97** 100801
- Girard C and Quidant R 2004 *Opt. Express* **12** 6141–6
- Glauber R J 1963 *Phys. Rev.* **130** 2529–39
- Golovko V B, Li H W, Kleinsorge B, Hofmann S, Geng J, Cantoro M, Yang Z, Jefferson D A, Johnson B F G, Huck W T S and Robertson J 2005 *Nanotechnology* **16** 1636–40
- Gordon M J and Peyrade D 2006 *Appl. Phys. Lett.* **89** 053112
- Hao E, Li S, Balley R C, Zou S, Schatz G C and Hupp J T 2004 *J. Phys. Chem. B* **108** 1224–9
- Haynes C L and Duynes R P V 2001 *J. Phys. Chem. B* **105** 5599–611
- Huang J X, Tao A R, Connor S, He R R and Yang P D 2006 *Nano Lett.* **6** 524–9
- Imura K, Nagahara T and Okamoto H 2004a *Chem. Phys. Lett.* **400** 500–5
- Imura K, Nagahara T and Okamoto H 2004b *J. Phys. Chem. B* **108** 16344–7
- Imura K, Nagahara T and Okamoto H 2004c *J. Am. Chem. Soc.* **126** 12730–1
- Jackson A M, Myerson J W and Stellacci F 2004 *Nat. Mater.* **3** 330–6
- Jin E X and Xu X 2004 *Japan. J. Appl. Phys.* **43** 407–17
- Johnson C J, Dujardin E, Davis S A, Murphy C J and Mann S 2002 *J. Mater. Chem.* **12** 1765–70

- Kelly K L, Coronado E, Zhao L L and Schatz G C 2003 *J. Phys. Chem. B* **107** 668–77
- Kinge S, Crego-Calama M and Reinhoudt D M 2008 *ChemPhysChem* **9** 20–42
- Klar T, Perner M, Grosse S, von Plessen G, Spirkl W and Feldmann J 1998 *Phys. Rev. Lett.* **80** 4249–52
- Krenn J R *et al* 1999a *Phys. Rev. Lett.* **82** 2590–3
- Krenn J R, Lamprecht B, Ditzlacher H, Schider G, Salerno M, Leitner A and Aussenegg F R 2002 *Europhys. Lett.* **60** 663–9
- Krenn J R, Weeber J C, Bourillot E, Dereux A, Goudonnet J P, Schider G, Leitner A, Aussenegg F R and Girard C 1999b *Phys. Rev. B* **60** 5029–33
- Krenn J R, Wolf R, Leitner A and Aussenegg F R 1997 *Opt. Commun.* **137** 46–50
- Landau L D and Lifshitz E M 1960 *Statistical Physics* 3rd edn (London: Pergamon)
- Law M, Sirbuly D J, Johnson J C, Goldberger J, Saykally R J and Yang P 2004 *Science* **305** 1269–73
- Lazarides A A and Schatz G C 2000 *J. Phys. Chem. B* **104** 460–7
- Lee K B, Kim E Y, Mirkin C A and Wolinsky S M 2004 *Nano Lett.* **4** 1869–72
- Lévêque G and Martin O J F 2008 *Phys. Rev. Lett.* **100** 117402
- Lin S, Li M, Dujardin E, Girard C and Mann S 2005 *Adv. Mater.* **17** 2553–9
- Linden S, Kuhl J and Giessen H 2001 *Phys. Rev. Lett.* **86** 4688–91
- Loudon R 2000 *The Quantum Theory of Light* 3rd edn (London: Oxford University Press)
- Maier S A, Brongersma M L, Kik P G, Meltzer S, Requicha A A G and Atwater H A 2001 *Adv. Mater.* **13** 1501–5
- Maier S A, Kik P G and Atwater H A 2003a *Phys. Rev. B* **67** 205402
- Maier S A, Kik P G, Atwater H A, Meltzer S, Koel B E and Requicha A A G 2003b *Nat. Mater.* **2** 229–32
- Maier S A, Kik P G and Atwater H A 2002 *Appl. Phys. Lett.* **81** 1714–6
- Martin O J F, Girard C and Dereux A 1995 *Phys. Rev. Lett.* **74** 526–9
- Mirkin C A, Letsinger R L, Mucic R C and Storhoff J J 1996 *Nature* **382** 607–9
- Mirkin C A, Letsinger R L, Mucic R C, Storhoff J J, Elghanian R and Taton T A 2007 *USA Patent* no 7259252
- Nelayah J, Kociak M, Stephan O, Garcia de Abajo F J, Tence M, Henrard L, Taverna D, Pastoriza-Santos I, Liz-Marzan L M and Colliex C 2007 *Nat. Phys.* **3** 348–53
- Novotny L 1996 *Appl. Phys. Lett.* **69** 3806–8
- Palik E D 1998 *Handbook of Optical Constants of Solids* (San Diego, CA: Academic)
- Passian A, Wig A, Lereu A L, Meriaudeau F, Thundat T and Ferrell T L 2004 *Appl. Phys. Lett.* **85** 3420–2
- Porto J A, Garcia-Vidal F J and Pendry J B 1999 *Phys. Rev. Lett.* **83** 2845–8
- Purcell E M and Pennypacker C R 1973 *Astrophys. J.* **186** 705–14
- Quidant R, Weeber J C, Dereux A, Peyrade D, Chen Y and Girard C 2002 *Europhys. Lett.* **65** 191–7
- Salerno M, Krenn J R, Hohenau A, Ditzlacher H, Schider G, Leitner A and Aussenegg F R 2005 *Opt. Commun.* **248** 543–9
- Smolyaninov I I, Massoni D L and Davis C C 1996 *Phys. Rev. Lett.* **77** 3877–80
- Tanaka S, Nakao M, Umeda M, Ito K, Nakamura S and Hatamura Y 2001 *J. Appl. Phys.* **89** 3547–53
- Tang Z Y, Kotov N A and Giersig M 2002 *Science* **297** 237–40
- Tao A R, Habas S and Yang P D 2008 *Small* **4** 310–25
- Tersoff J and Hamann D R 1985 *Phys. Rev. B* **31** 805–13
- Thomas K G, Barazzouk S, Ipe B I, Joseph S T S and Kamat P V 2004 *J. Phys. Chem. B* **108** 13066–8
- Vlasov Y A, Bo X Z, Sturm J C and Norris D J 2001 *Nature* **414** 289–93
- Weeber J C, Krenn J R, Dereux A, Lamprecht B, Lacroute Y and Goudonnet J P 2001 *Phys. Rev. B* **64** 045411
- Wiederrecht G P 2004 *Eur. Phys. J. Appl. Phys.* **28** 3–18
- Wurtz G A, Im J S, Gray S K and Wiederrecht G P 2003 *J. Phys. Chem. B* **107** 14191–8
- Zayats A V and Smolyaninov I I 2003 *J. Opt. A: Pure Appl. Opt.* **5** S16–50
- Zhang H, Edwards E W, Wang D Y and Mohwald H 2006 *Phys. Chem. Chem. Phys.* **8** 3288–99